Applied Energy 332 (2023) 120395

Contents lists available at ScienceDirect

Applied Energy

journal homepage: www.elsevier.com/locate/apenergy

Influence of the anode overhang on the open-circuit voltage and the ageing of lithium-ion batteries—A model based study

Felix Hildenbrand [a,*], Dominik Ditscheid [a], Elias Barbers [a,b,c], Dirk Uwe Sauer [a,b,c]

[a] ISEA RWTH, Campus Boulevard 89, Aachen, 52074, Germany
[b] Helmholtz Institute Muenster (HI MS), IEK-12, Forschungszentrum Juelich, Campus Boulevard 89, Aachen, 52074, Germany
[c] JARA-Energy, Juelich, 52425, Germany

ARTICLE INFO

Keywords:
Ageing model
Anode overhang
Bayesian optimisation
Lithium-ion batteries
Machine learning

ABSTRACT

The anode overhang has been proven to be a non-negligible influencing factor in the ageing trajectory of lithium-ion batteries. It acts through the transfer of active lithium between the anode overhang and the active anode by changing reversibly the cell balancing. In this work, the anode overhang is proven to influence the open-circuit voltage. Through a high-precision measurement, a persistent rise of the open-circuit voltage was observed, which we have demonstrated to originate in the anode overhang effect. The dimensions and structure of the anode overhang were verified by a post-mortem analysis of the cell and matched with the voltage behaviour. Derived from this finding, an existing electrical–thermal ageing model was extended to allow the simulation of the interaction between the anode overhang and the capacity. With a Bayesian optimisation approach, the extended model allowed to drastically improve model parametrisation when ageing test data include an increase in capacity. The resulting model was verified with the simulation of two ageing profiles, each including varying ageing conditions and phases of capacity recovery. The model allows ageing predictions with a deviation below 4% of the remaining capacity after more than 750 days of ageing. The model is publicly available as part of an open-source project.

1. Introduction

As electrochemical active systems, lithium-ion batteries (LIBs) are subject to permanent degradation. The degradation or ageing takes the form of decreasing capacity or increasing inner resistance. The degradation results in a reduction of energy or power capability. The rate of degradation and how the degradation is influenced by operating conditions have been the subject of various ageing studies [1–9]. By the means of empirical or semi-empirical ageing models, the results of these ageing studies were made available for the ageing investigation of real-world applications.

Recent findings showed that lost capacity can be recovered [5,10] leading to a differentiation between reversible and irreversible capacity loss. The effect of the anode overhang (AOH) is a prominent driver for reversible capacity loss. The AOH influences the early capacity trajectory in ageing studies where static state-of-charge (SOC) in calendaric ageing or fixed average SOC in cyclic ageing are tested [11,12]. Hence, the influence of the AOH can lead to misinterpretation of ageing test results [10,13,14], resulting in a need for special consideration of the AOH in ageing data analysis. Wilhelm et al. [13] showed how the effect could be tracked via the coulombic efficiency (CE) in repeated cycling. Burrel et al. [14] showed that the effect of the AOH distorts the results of a cycling ageing study if the duration of constant-voltage (CV) charge phases differs for the test points. Lewerenz et al. discussed in [10] how the effect of the AOH hides the irreversible ageing trajectory and presented an approach to find the actual ageing trajectory by including resting periods into the test. Furthermore, the same author showed that the homogeneity of lithium distribution (HLD) is a further major source of reversible capacity loss on the negative electrode, also being influenced by resting periods [15,16].

For a correct evaluation of ageing test results, a systematic approach integrating the knowledge about the AOH effect is required. The AOH is the area of the anode lacking a geometrically opposed cathode, therefore it cannot directly take part in the charging and discharging process. The AOH is also described as the passive anode, while the part of the anode with an opposed cathode is called the active anode. The AOH can be understood as a reservoir of active lithium connected to the active anode [11]. The transfer of active lithium from the AOH to the active anode and back modifies the available lithium inventory for cycling. Thus, the cell balancing is changed, changing the cell capacity. The average test SOC is the main driver of the AOH-effect on the

---

[*] Corresponding author.
E-mail address: felix.hildenbrand@isea.rwth-aachen.de (F. Hildenbrand).

https://doi.org/10.1016/j.apenergy.2022.120395
Received 4 August 2022; Received in revised form 6 November 2022; Accepted 18 November 2022

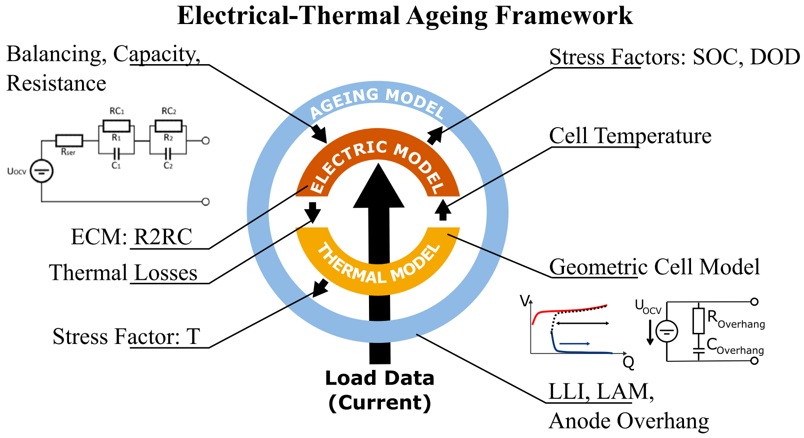

Fig. 1. Structure of the framework and interactions between the sub-models.

capacity [12,14] and the CE [11,13]. The exchange process between the active and passive anode is operated by the transport of ions through the electrolyte [13] and can be influenced by the properties of the separator [17]. The exchange process is accelerated towards elevated temperatures [12,18]. The geometry of the AOH influences the exchange through size and distance of the passive to the active anode areas [17,18]. As these are all cell design parameters, the influence of the AOH can be expected to be different for every cell type. Finally, the effect of the AOH has been proven to impact the comparison of capacities extracted at different C-rates [15,17].

In order to combine the factors influencing the effect of the AOH numerous models have been developed. Warnecke [19] and Hüfner et al. [18] presented a lumped circuit model of the passive anode area, connected to the active area. The circuit models an ionic current. The model presented by Hüfner resolved different areas of the passive anode by parallel circuits. A Newman-type 0D-electrochemical model was presented by Fath et al. [17]. This model resolved different areas of the anode overhang by superposition. Schmalstieg et al. [20] integrated the passive anode in a pseudo-2D-electrochemical model and showed that it allowed simulating the effect of the AOH.

The model presented in [20] was the only one allowing a combination with other ageing effects while the other models presented an isolated consideration of the AOH effect. Ageing data is often analysed and modelled using a simpler empirical approach [2,6,8], leading to an over-simplified representation of the actual degradation trajectory which does not consider the effect of the AOH present in the data. A model that integrates the AOH into an empirical ageing model would allow for improving the ageing data analysis and representation. Further, it would enable a more accurate degradation trajectory modelling of real-world applications. Real-world applications are influenced by the AOH in resting periods such as parking of EVs, changing average SOC in the operation of a home-storage system or in vehicle-to-grid scenarios [21], including the AOH would allow reducing the divergence between simulated degradation and degradation measured in the field.

To address these issues the authors pursued the questions of how the AOH effect can be integrated into an empirical ageing model and how could such a model be parametrised accurately. These reflections led to the question, of whether the effect of the passive anode can be measured directly in cell voltage rather than as a disturbance of the capacity or the CE. This paper addresses these questions by first demonstrating the influence of the anode overhang on the open-circuit voltage (OCV). Then, an empirical ageing model with a machine learning-based parametrisation method is presented. The model is verified with sequences of ageing tests including points of capacity recovery. Finally, the remaining deviations between the measured ageing trajectory and the model output are analysed, and the model limits are elucidated.

2. Experimental

2.1. Cell characterisation

The lithium-ion battery (LIB) investigated in this work was a prismatic NMC111-graphite cell manufactured by Samsung SDI, with a nominal capacity of 94 Ah. The cell is of type high energy and used in stationary energy storage applications. The four investigated cells were commercially acquired. To investigate the cell characteristics, one cell was disassembled in an Ar-filled glove box. Before disassembling, the cell was discharged to the end of discharge voltage (EODV) with a current of 1.88 A (C/50). The electrode sheet dimensions and coating surfaces were measured using a measuring tape with a precision of 0.5 mm. Single electrode voltage curves were determined using half-cells built in coin-cells with lithium metal counter-electrodes and a glass-fibre separator. The differential voltage analysis (DVA) of the half-cell's quasi-open-circuit voltage (QOCV)-curves allowed assigning of the full-cell's DVA peaks to the electrodes. The electrode chemistry was verified by inductively coupled plasma - optical emission spectrometry (ICP-OES).

2.2. Ageing tests

The ageing data to parametrise the ageing model was extracted from a manufacturer data-sheet. The ageing conditions are listed in Table 1. For verification purposes, ageing data distinct from the parametrisation data was used. Two verification profiles were measured: profile 1 and profile 2. The profiles were composed of test sequences of approx. 30 days. Each sequence had fixed test conditions with mean SOC, depth-of-discharge (DOD) and temperature. The values of the test conditions were chosen randomly within the range of real-world applications and intentionally differed from parametrisation test conditions. At each sequence transition, the tested cells underwent a check-up (CU) including a capacity test. After the CU the test conditions could be changed. Profile 1 was applied to cell 1 and profile 2 was applied to cell 2. Cell 3 underwent an ageing test which cannot be disclosed, the relative capacity at the end of this test was 94%. The OCV voltage measurements were performed after completing the ageing tests.

2.3. Electrical tests

All charge and discharge operations were performed using Digatron MCT-100-06-12 ME. All SOCs were set using Ah-counting, relative to the last discharged capacity. For temperature conditioning in all tests, the cells were placed in a Binder 53L climate chamber. To parametrise the equivalent circuit model (ECM), electrochemical impedance spectroscopy (EIS) measurements were performed using a Digatron EISmeter. The measurements were done at 21 equidistant SOC levels between 0 and 100%. The EIS were performed at four temperatures: 5 °C, 15 °C, 25 °C and 35 °C. QOCV-curves were measured at the aforementioned temperatures with a current-rate (C-rate) of C/20. To parametrise the anode overhang model OCV voltage measurements were performed during rest periods of 10 to 25 days and in the case of cell 3 for a rest period of > 150 days. Due to constraints of experimental equipment, the measurement could not start right after the setting of the lowest SOC at EODV, but with a few days of delay as indicated in Fig. 2(a). The duration of the resting periods were selected in accordance with the observed voltage evolution, allowing us to observe the effect of the voltage whilst shortening the experiment. Cells 1 and 2 were rested at the following voltage levels: 3 V, 3.4 V, 3.55 V, 3.7 V, 3.9 V and 4.15 V. The cells were first discharged to the EODV and then step-by-step charged with a constant current of C/10 to the resting voltage levels. Cell 3 remained at the lowest level, in order to get a data point for the long-term evolution. The voltage levels and their resting duration are displayed in Fig. 2(a). The voltage was measured with a precision of 100 μV using a custom build voltage logger. The voltage was sampled every two hours. In-between measurements, the LIBs were disconnected from the measurement circuit by a relay to prevent the possibility of any leakage currents. The tests were performed at a constant temperature of 35 °C. The resting tests were performed on the three cells after long-term ageing tests.

3. Model

The presented model was developed on the basis of an electrical–thermal ageing framework, referred to hereafter as ‘framework’, developed at our institution and available as an open source project [22]. The purpose of the model is to combine the short-term electrical–thermal application level of the LIB with the long-term ageing level. The model is split into three sub-models, each of which is parametrised individually. This approach was first presented by Schmalstieg et al. [2]. Fig. 1 gives a schematic description of the model, with an overview of the sub-models. The model is implemented in C++, for details of the implementation the reader should refer to the work of Hust [23]. Matlab including the optimisation toolbox was used for data processing, parametrisation and optimisations.

3.1. Electrical–thermal model

The electrical–thermal model is the core of the framework. The simulation input is a load profile expressed as current over time. The current profile is processed within the electrical model, composed of two half-cell OCV-curves and an ECM consisting of a serial resistance and two RC-circuits (see Fig. 1). A simple ECM was selected as the focus of this work was the ageing simulation. The split in two half-cell OCV-curves accommodate a changing cell balancing. All values of the electrical model are temperature and SOC dependant, the exact values are provided by look-up tables. The model was parametrised through the fit of the R2RC-Model to the results of EIS-measurements and current pulse tests. The electrical simulation and the thermal simulation are executed in alternating steps to account for their mutual interaction. The thermal model of the cell is a prismatic thermal block of active material with anisotropic heat conductivity. The conductivity is higher along the current collectors. The heat dissipated by the ohmic resistance of the electrical model in the thermal block is exchanged with the environment at a constant temperature. This is a simplified model of the test situation in a climate chamber.

3.2. Ageing model

The used ageing model was based on the ageing functions presented by Schmalstieg et al. [2]. The ageing model has a two-level structure. The first level describes the capacity and resistance trajectories with regard to time and charge throughput. In contrast to Schmalstieg et al. a linear function was used to describe the trajectories. The second level describes how the coefficients of the first level linear function depend on the stress factors influencing the LIB ageing. The second level was described by the following functions, returning the linear coefficients α for calendaric and β for cyclic ageing.
Calendaric Ageing:

$$\alpha = (a_1 + a_2 \cdot SOC) \cdot e^{-\frac{a_3}{T}} \tag{1}$$

Cyclic Ageing:

$$\beta = b_1 \cdot (\overline{SOC} + b_2)^2 + b_3 \cdot \Delta DOD + b_4 \tag{2}$$

The calendaric ageing is a function of the stress factors temperature (T) and SOC. The cyclic ageing was a function of the stress factor’s average SOC over the cycles and DOD. In order to account for micro and macro cycles, the DOD values were calculated via a rainflow algorithm. All model input values of the stress factors were calculated as averages of the values returned in the electrical–thermal model. The averages were calculated for a fixed ageing step of one day. For a detailed description of the parameters, the reader should refer to the original publication of the model [2]. The model was initially parametrised through an individual fit of the capacity and resistance trajectories of calendaric and cyclic ageing tests with a linear function. Points deviating substantially from the linear trajectory were excluded from the initial fit. Deviations in the capacity in early life were covered in the AOH model. Deviations in later life, which were attributed to the rollover effect [24], were out of the scope of this model. The generated linear coefficients were used to fit the function (1) and (2) using a non-linear least square fit. The start values for the global fit were evaluated using single stress factor fitting. The changes in resistance were mapped to the serial resistance of the impedance model. The changes in capacity were mapped to anode and cathode capacity, and to the lithium inventory, defined by the cell balancing. The differentiation between loss of electrode capacity and lithium inventory in modelling ageing of LIBs was applied to calendaric ageing in the recent publication by Montaru et al. [25].

3.3. Anode Overhang Model

The AOH was modelled as a lumped electrical circuit, representing the lithium-ion flow between the active and the passive anode area [18, 19]. While the active part was modelled through a non-linear voltage source, parametrised by the anode half-cell OCV-curve, the passive part was modelled by a capacitance and a resistance representing the size of the ion reservoir and the hindrance to ionic conduction, respectively. Thus, the electric circuit formed a serial RC element. The RC circuit was connected to a virtual lithium inventory which determines the balancing between anode and cathode half-cell curves. Through changes in the balancing, the AOH affected the full-cell capacity. The simulation of the AOH was executed as part of the ageing simulation. As the AOH is modelled as RC circuit connected to a “voltage source”, the exchange between AOH and the active anode can be described by the following expression:

$$\Delta Charge_{Li}(t) = C_{AOH} \cdot (V_{OH} - V_{Anode}) \cdot (1 - e^{-\frac{t}{\tau_{AOH}}}) \tag{3}$$

Where $\Delta Charge_{Li}$ is a current of ions, with the unit A and C_{AOH} is the modelled capacitance of the anode overhang, which is approximated by the slope of the anode’s QOCV-curve. Following [19] we assumed an Arrhenius-dependency for the time constant of the AOH:

$$\tau_{AOH} = c_1 \cdot e^{\frac{C_2}{T}} \tag{4}$$

Table 1
Ageing conditions of the calendaric (Cal.) and cyclic (Cyc.) ageing data used for the model parametrisation. For each condition, data of a single ageing trajectory was available.

Test condition ID	Ageing type	Temperature	SOC (mean)	DOD	Current charge	Current discharge
		°C	%	%	C	C
A01	Cal.	60	100	–	–	–
A02	Cal.	60	70	–	–	–
A03	Cal.	60	40	–	–	–
A04	Cal.	60	10	–	–	–
A05	Cal.	10	100	–	–	–
A06	Cal.	25	100	–	–	–
A07	Cal.	50	100	–	–	–
B01	Cyc.	25	50	100	0.5	1
B02	Cyc.	15	50	100	0.5	1
B03	Cyc.	25	87.5	25	0.5	1
B04	Cyc.	25	62.5	25	0.5	1
B05	Cyc.	25	37.5	25	0.5	1
B06	Cyc.	25	12.5	25	0.5	1
B07	Cyc.	35	50	100	0.5	1
B08	Cyc.	45	50	100	0.5	1
B09	Cyc.	5	50	100	0.5	1
B10	Cyc.	25	75	50	0.5	1
B11	Cyc.	25	50	50	0.5	1
B12	Cyc.	25	25	50	0.5	1

The first parameter c_1 is attributed to the geometry of the AOH while the second one c_2 is material related. The parametrisation was initially done through a fit of the RC-circuit to the OCV measured during resting at different SOC points. This allowed to extract an average time constant τ, valid for all SOCs, while the temperature dependency was neglected.

3.4. Global optimisation

In order to improve the quality of the ageing model a global optimisation of the parameters was setup. The idea was to improve the interaction of the ageing sub-models: the calendaric, the cyclic and the AOH model. We used the Bayesian optimisation approach which relies on Gaussian process regression to model the dependency between the target variable and the input variables [26]. The optimisation goal was to minimise the deviation between the capacity curve of the ageing tests and the simulation result at each specific condition listed in Table 1. In each iteration of the optimisation, the ageing tests were simulated with the framework. The model parameters in (1), (2) and (3) were used as input variables. To quantify the goodness of the simulation the mean-square error (MSE) of the relative capacity between original data and simulated ageing was calculated as follows:

$$MSE_{Cond.} = \frac{1}{n}\sum_{i=0}^{n}(Cap_{Model,i} - Cap_{Meas.,i})^2 \tag{5}$$

The MSEs of each condition were combined in a global root-mean-square error (RMSE) that minimises the deviation of all conditions. The target variable was calculated as follows:

$$RMSE_{Glob.} = \sqrt{\frac{1}{n}\sum_{i=0}^{n} MSE_{Cond.,i}} \tag{6}$$

With n being the number of different ageing conditions.

The optimisation was implemented in Matlab (r2021b), calling the framework as an executable compiled for Windows. Each iteration of the Bayesian optimisation had the following structure: First, all ageing conditions were simulated using a parallel computing setup. Second, the simulation results were evaluated against the original data and the single MSE values were calculated. Based on the global $RMSE_{All}$ calculated via Eq. (6), the next parameters for a new iteration were selected. For the selection, a Gaussian process was trained. A variant of the expected improvement algorithm was used to pick the next model parameters for a tryout, based on the Gaussian process. The optimisation was limited to 400 evaluations for each ageing condition. More iterations did not significantly improve the result. The bounds for the parameters in (1) and (2) were selected to limit the search area between the minimal (0 Ah/day) and maximal ageing (0.094 Ah/day). The lower limit is motivated by the fact these equations do not allow capacity gain. The upper limit is motivated by the fact that a capacity loss of more than 1% of the nominal capacity per day was not observed in the training data.

4. Results and discussion

4.1. Investigation of the open-circuit voltage

As the AOH influences the extractable capacity of a LIB we conjectured that the OCV should be affected by the transfer of ions between the active and the passive part of the electrode. The OCV is, after a sufficient resting period of the LIB, a function of the lithiation degree of both electrodes and the temperature. Hence, an increase of the active lithium in the active anode should be detectable in the cell voltage. Through the measurement of the OCV at different SOCs, we observed a significant and persistent change of the voltage during resting in dependence on the initial set SOC, as depicted in Fig. 2. The observed voltage changes are in the range of 5 to 50 mV. For a SOC close to 0% we can observe a voltage increase (Fig. 2(b)–(d)). Self-discharge can be excluded as an explanation for this behaviour of the OCV as the voltage increases, which is not an energetically favoured behaviour. A charge through the measurement device can be excluded as the cell was disconnected via a relay from the device during the resting time, except for 20 s measurement time every two hours. We concluded that the voltage rise must be linked to a redistribution of Li-ions between the active anode and the AOH. This confirms the observation of Zilbermann et al. [27], who reported an influence of the AOH on the self-discharge measurements via OCV-measurements.

For the long-term measurement of cell 3, the detail in 2(b) shows an increase in two steps. The first step was completed after approximately ten days. The second step took over 100 days to complete. The voltage behaviour matched perfectly our findings in the post-mortem study. We found a jelly roll composed of four wound coils, electrically connected in parallel at the tabs. Each of the coils presented two longitudinal and two lateral negative electrode areas without opposite positive electrode, forming together the AOH (see Fig. 3(b) and (c)). The AOH was 9% of the total anode active surface (859 cm^2 out of 9567 cm^2 per coil).

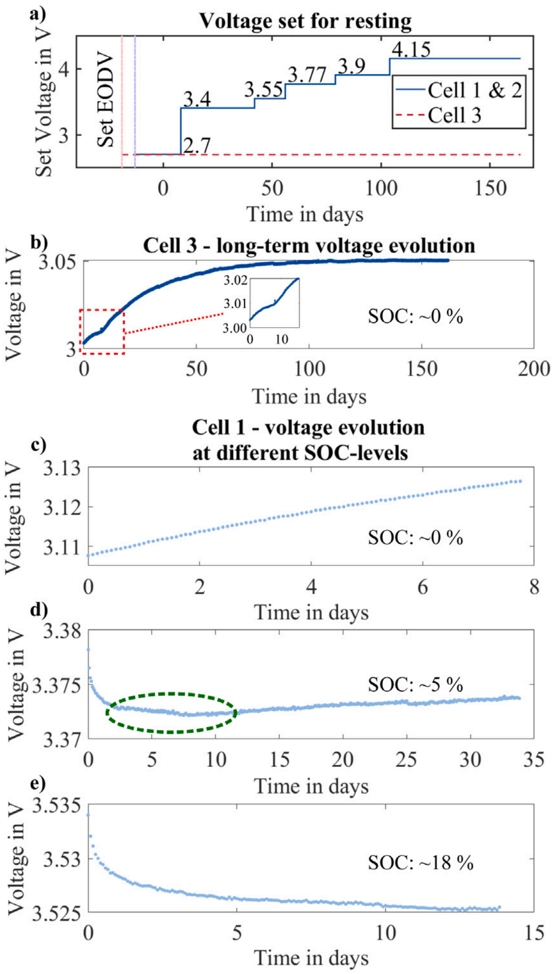

Fig. 2. After setting the voltage by CC-charging to different levels indicated in (a), the OCV was measured for consecutive resting periods (b)–(e). For all plots, the indicated time is set to 0 at the beginning of the voltage measurements.

The AOH area was composed of a much smaller longitudinal area (178 cm^2 per coil), which was connected over a larger distance to the active area. This would allow a fast but short exchange of the active lithium. Further, it was composed of a bigger lateral area (681 cm^2 per coil), with only the lateral width of the coil connecting to the active area. We divided the AOH into two types of areas, as depicted in Fig. 3(c): the well-connected but small "near" AOH and the bigger but significantly less connected "far" AOH. We associated the two AOHs with the two phases of the voltage evolution as depicted in Fig. 3(d), the near AOH with short-term change (<10 days) and the far AOH with long-term change (>100 days).

Cells 1 and 2 were stepwise charged to higher SOCs with a C-rate of C/10. The start of the measurement on cell 1 at 0% SOC (Fig. 2(c)) was delayed after the discharge to EODV, hence the voltage had already time to recover. Voltage recovery after discharge is influenced by the remaining capacity and the internal resistance of the cell. In this case, the SOH of cells 1 and 2 was lower than the one of cell 3, hence the voltage rose higher during the relaxation after discharge. This means that the voltage of cell 1 starts higher than the one of cell 3. On the following SOC level of 5%, the voltage trajectory displayed three phases (Fig. 2(c) and 3(d)). First, the voltage had been dropping sharply for two days, then it had been decreasing with a smaller gradient for eight days until it reached a minimum, marked with a green circle in Fig. 2(c). The initial drop was associated with the relaxation after the charge. The second phase was associated with the equalisation of the near AOH and the third phase was associated with the equalisation of the far AOH areas. Finally, the voltage started to rise again. For SOC 18% and all higher SOCs, the voltage measured was always decreasing. Here, the voltage decrease stabilised to values between 70 $\frac{\mu\text{V}}{\text{day}}$ at 3.9 V, and 180 $\frac{\mu\text{V}}{\text{day}}$ at 4.1 V (after 10 days). All further SOC levels showed the same tendency and are therefore not shown here. Fig. 4 displays the li-ion-exchange for the three cases.

We assumed that the SOC of both AOH areas, near and far, were at a SOC above 10% before the experiment. Due to the complex cycling history, an exact estimation was not possible. The resting at 0% at the beginning of the experiment discharged the AOH. The near AOH fully released its lithium content to the active part. For the far AOH, hosting much more lithium, the process was too slow to empty it completely. During the resting at 5%, the near AOH was refilled with lithium, hence the observed cell voltage decreased. After the near AOH was lithiated to the same level as the active part, the cell voltage rose again. The voltage rise was driven by the lithium transferred from the far AOH, which still retained a SOC above 5%. For all SOC levels from 18% upwards, only a cell voltage decrease was observed. The combination of two factors led to the decrease. First, the anode OCV had little to no gradient in the area of the set voltages (3.55 V, 3.7 V, 3.9 V and 4.15 V). Thus, a change in lithiation of the active anode would not lead to a change in the cell voltage. Second, with increasing SOC, the SOC of the active anode area approached and eventually surpassed the SOC of the AOH. This reduced and inverted the driving force for the transfer of active lithium from the active part to the AOH. The amount of transferred lithium got smaller and when the trend was inverted, the effect of the transfer could not be differentiated from the self-discharge [27,28].

4.2. *Modelling of the AOH charge and discharge*

The curve of the OCV during resting was used to parametrise a model of the AOH charge and discharge. Fig. 3(e) depicts the fitted RC-circuit model composed of three serial RC elements connected in parallel. The first element, RC Relax, is used to model the relaxation process in the fit but was not part of the final model. The relaxation was simulated by the impedance model. The RC near element was fitted with a time constant in the range of 3 to 15 days. The RC far element was fitted with a time constant above 50 days. The fit was done at the three lowest SOC levels for cells 1 and 2 (0%, 5%, 18%). Fig. 3(d) depicts the fit for cell 1 at a starting SOC of 5%. The model was not SOC-dependent but was parametrised with average values of the time constants of the three lowest SOC levels.

For verification purposes, the model was used to simulate the long-term voltage evolution of cell 3, which was not used to parametrise the model. Fig. 3(f) depicts the result. The simulation follows the measured voltage curve. The initial deviation was due to the unknown initial SOC of both AOH areas, which made it unfeasible to get the right starting point. The difference in the long-term trend was attributed to the reversible self-discharge [27] which is overlaid to AOH equalisation, while it was not implemented into the model.

4.3. *Ageing model optimisation*

The initially parametrised AOH model was integrated into the framework as part of the ageing model. The improvement in the model performance was investigated by simulating the parametrisation data. Fig. 5 displays the square root of the $MSE_{cond.}$ as defined in (5) between the simulation and the measurement for different test conditions and different model configurations. For the benchmark, the initially parametrised ageing model without AOH model, we observed a strong initial deviation. Adding the AOH model improved especially the calendaric tests at high temperatures (A1–A4). This was explained by the stronger impact of the AOH due to a faster exchange between the active anode and AOH at higher temperatures. But the overall performance in all ageing conditions left room for improvement. To

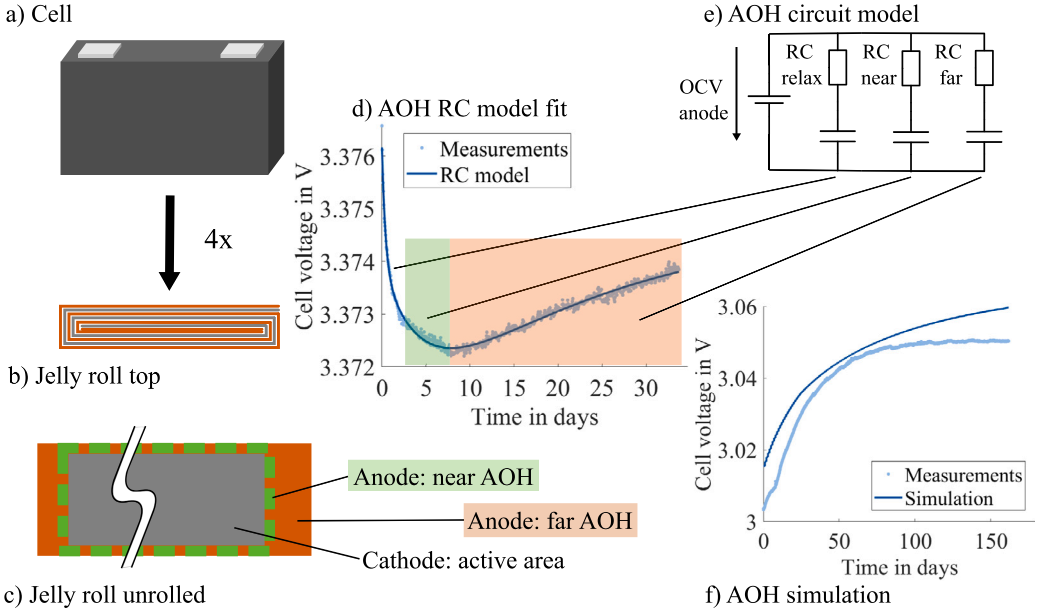

Fig. 3. Geometry of the anode overhang and its effect on the open circuit voltage.

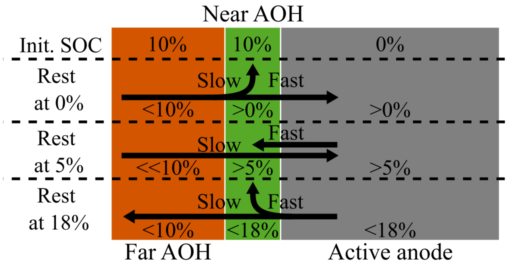

Fig. 4. Schematic exchange of active lithium between the active anode, the far and the near AOH area for cell 1. The initial SOC is indicated for the moment right after the discharge to the EODV. At each SOC level, the approximate SOC is indicated, which was reached right before the change of SOC.

enhance the interaction between the models we proposed a combined parametrisation of the ageing model and AOH model, through global optimisation. The goal of the optimisation was to reduce the deviation between the measured and the simulated ageing trajectories for the ageing conditions in Table 1 by modifying the parameters of the ageing Eqs. (1), (2) and (4). To keep the number of the optimised parameters as small as possible in one optimisation pass, the optimisation was split into several passes. The parameters of the calendaric ageing model and AOH were optimised together in a first optimisation pass. The optimisation lead to substantial improvement and allowed us to push the RMSE to under 1%-point of relative capacity for all calendaric test conditions (Fig. 5(a)). In the second pass, the cyclic ageing model parameters were optimised, using the calendaric and the AOH model with the parameters from the previous optimisation round.

While the second optimisation pass improved most of the conditions, especially at low temperatures in the cyclic ageing (B02, B09) the model was still showing a strong deviation. We decided to integrate the effect of the temperature on the cyclic ageing in the model by extending Eq. (2) as follows:

$$\beta = b_1 \cdot (\overline{SOC} + b_2)^2 + b_3 \cdot \Delta DOD + b_4 + b_5 \cdot (\overline{T} - b_6)^2 \tag{7}$$

We chose a second-order polynomial dependency following [29]. The optimisation was repeated with the new ageing function. It allowed pushing the RMSE for all cyclic conditions below 3%-points of relative capacity. Meanwhile, it also reduced accuracy in some points, most significantly at 100% DOD and 50% SOC (B01). This indicated an initial over-fitting on this single condition. The reduction was considered an acceptable trade-off, as we were seeking a globally good model. The optimisation returned a temperature for minimal cyclic ageing of 23.6 °C (parameter b_6 in Eq. (7)). This was in line with the results of Waldmann et al. [29], who found a minimal cyclic ageing little below 25 °C. Our result was below the value found by Werner et al. [30], who found a minimal cyclic capacity loss at 32 °C but investigated a different cell chemistry (LCO/NCA-graphite).

4.4. Ageing model verification

The model was verified with two sequences of ageing tests including a great variety of ageing conditions (see Fig. 6(a) and (b)). The current profile measured during the tests was used as the sole input for the simulation. The measured capacity trajectories of both sequences depicted as black crosses in Fig. 6(c) and (d) show changing ageing rates including periods of recovery. The model returned a continuous capacity, depicted as a line. Obviously, capacity values are not continuously measurable. For the comparison between the model and the measurements, the capacity returned by the model at the moment of the check-up is marked with circles. The initial parametrisation of the model resulted in much weaker ageing than measured. Optimising the model and adding the temperature dependency for the cyclic ageing increased the overall ageing and substantially improved the estimation accuracy. The simulation was capable of reproducing variations of the ageing rate and recovery of the capacity, hence the model is suitable for complex ageing trajectories as measured in the two reference ageing tests. Further, the model allowed to access the SOC of the AOH which is a hidden parameter, not accessible by direct measurement in the CU during the ageing test. Fig. 8(a) depicts the evolution of the SOC of both AOH and (b) depicts the cumulated lithium transferred from the AOH to the active anode and back. Both values were calculated by Eq. (3), cumulating the exchanged lithium, starting from defined AOH SOCs at the beginning of the test. The far AOH was estimated at around 40% SOC (likely SOC after formation) at the beginning of the test. Resulting in the active anode gaining lithium from the far AOH throughout the whole test. The near AOH SOC was estimated to be around 0% at the beginning of the test, as the LIBs were stored at 0% SOC shortly before the test. The near AOH is discharged in a very short time, as shown before. The charge was mostly transferred from the active part to the

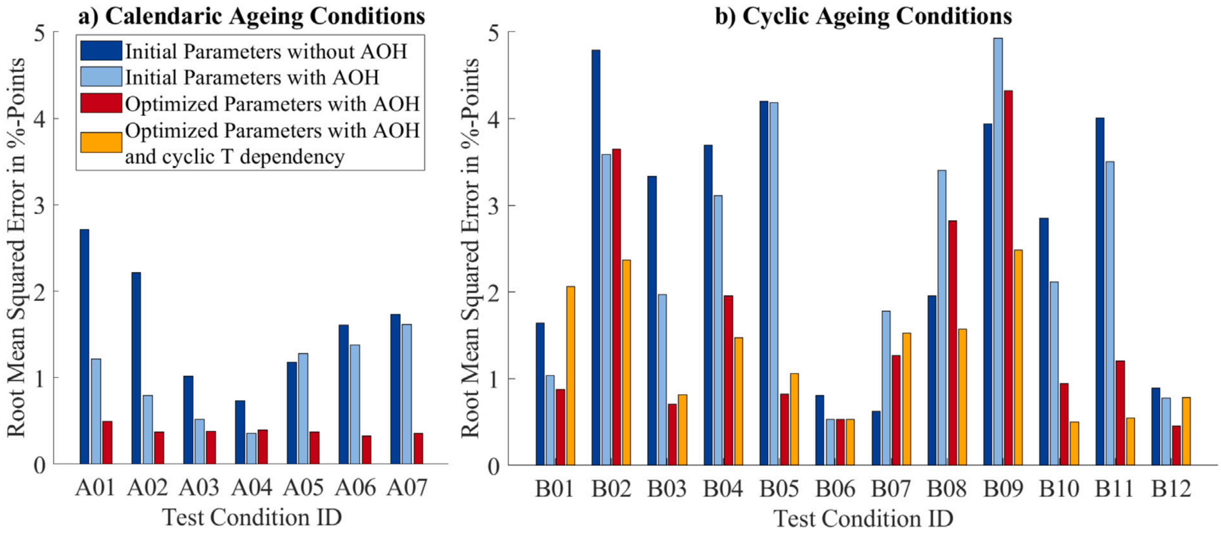

Fig. 5. Results of the model parametrisation. (a) and (b) depict the RMSE between measured and simulated relative capacity for the different ageing tests used in the model parametrisation. The RMSE is expressed in %-points as it is calculated for relative capacity values in %. The colours describe the different expansion states of the ageing model.

near AOH. Being then transferred back, leading to an entirely negative cumulated-transferred lithium.

For profile 1, the final measured capacity was estimated with a deviation of 0.99 Ah for a lost capacity of 9.97 Ah. Put in relation to the actual capacity in the last CU of 83.86 Ah, this resulted in a relative error of 1.18%, after 778 days of simulated load profile. For profile 2, the deviation was 2.84 Ah for 13.78 Ah of lost capacity. Put in relation to the actual capacity in the last CU of 79.91 Ah, this resulted in a relative error of 3.57%, after 776 days of simulated load profile. Over the course of the simulation, the deviation accumulates, hence the final deviation is a sweeping value. In Fig. 6, four segments are marked where the changes in capacity differ strongly between simulation and measurement. In the case of profile 1, the test and simulation diverged between CU 5 and CU 6, with a stronger loss of capacity than in the simulation (marker 1). The trajectories of the simulation and the test converged again after a strong capacity increase between CU 10 and CU 12 (marker 2). In the case of profile 2, the capacity deviates strongly between CU 3 and 4 (marker 3) and later drops after CU 7 (marker 4). In order to understand the origin of the model's inaccuracy, we performed a differential voltage analysis on the test data for the affected segments of the test.

4.5. Model limitations

Since the model and the measurement converged again after deviating, we established the hypothesis stating that the deviations originated in reversible effects not included in the model. Reversible capacity loss can be attributed to the transfer of active lithium to the AOH or to the reduction of the cell's homogeneity, the second of which is not included in the model. By performing a differential voltage analysis and tracking the peaks in the $\frac{dV}{dQ}$ curve the recovery of capacity can be attributed to either of the effects. In Fig. 7(a), the tracked peaks of

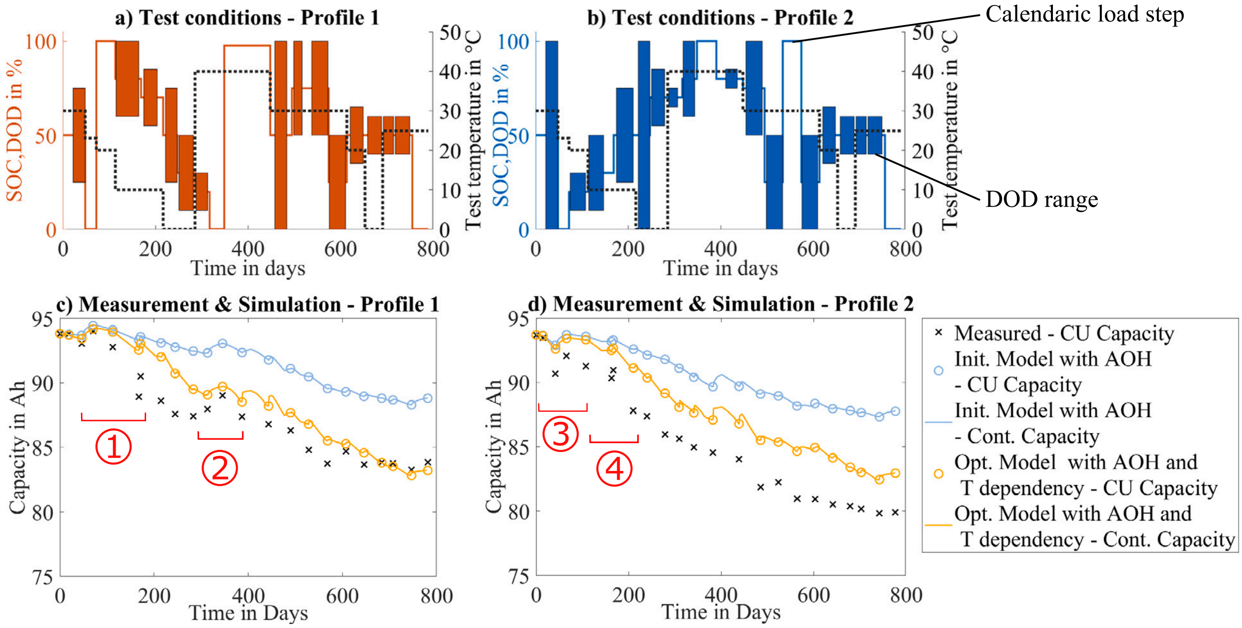

Fig. 6. Model verification profiles applied on cell 1 and cell 2. (a) and (b) depicts the load conditions in each step, (c) and (d) the measured and the simulated capacity with the initial and the optimised models. For the simulated capacity trajectories, the continuous capacity (cont. capacity) and the capacity at the check-up (CU capacity) are displayed. Except for the simulated capacity trajectory of the initial model without AOH, where we left the CU capacity out for more clarity.

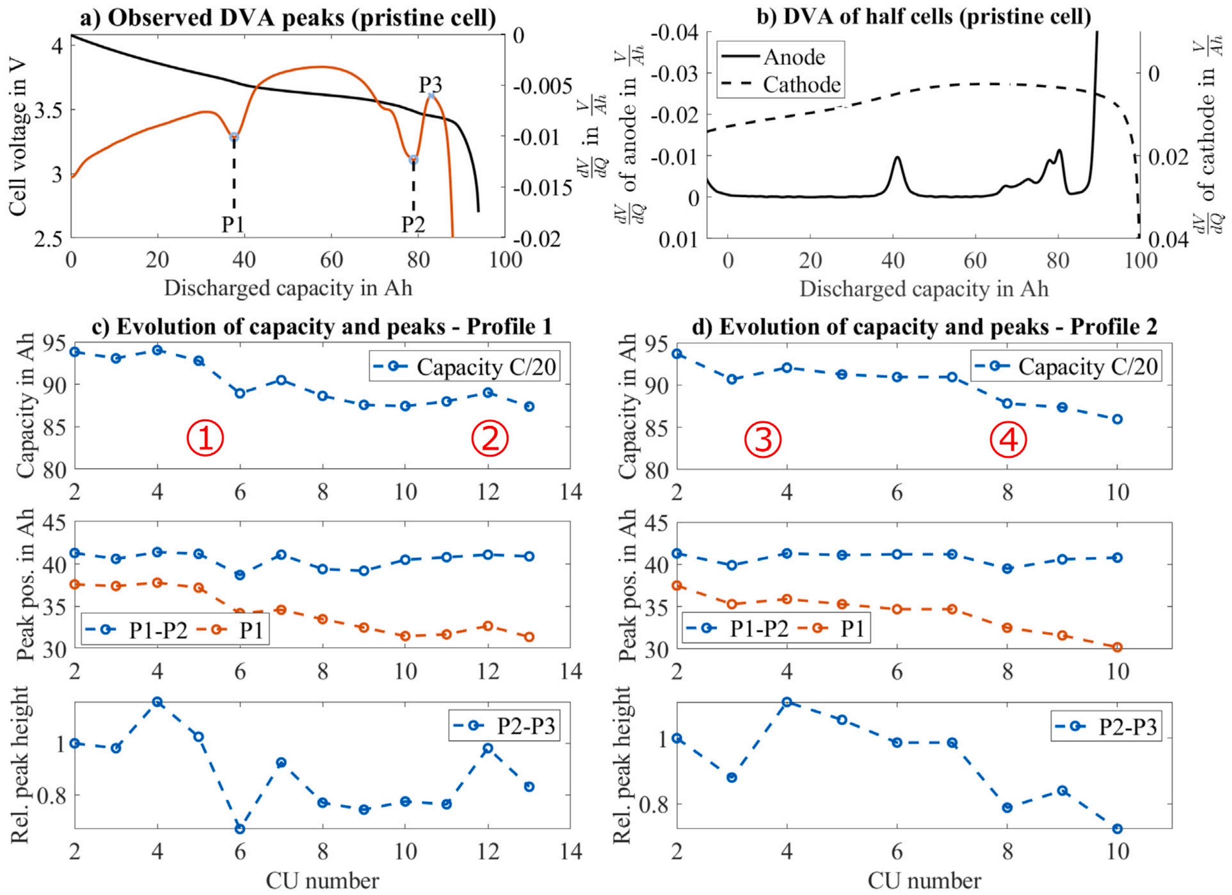

Fig. 7. Analysis of the deviation between model and verification profile. The position, the relative distance and the relative height of the peaks indicate the source of the capacity loss and gain. Prominent points are marked with number 1–4. For identification of the peaks, the QOCV- and DVA-curves of the full-cell as well as the DVA-curves of the half-cells are plotted in (a) and (b). In (b), to facilitate comparison, the half-cell capacity was scaled to the full-cell capacity and the y-axis for the anode curve was inverted.

the DVA are defined. In Fig. 7(c) and (d) display the evolution of the full-cell capacity, the distance of P1 to the fully charged cell (P1), the distance between P1 and P2 (P1–P2), and the vertical distance between P2 and P3 (P2–P3). All values are relative to the values in CU 2. All marked peaks are part of the anode voltage characteristic. P1 quantifies the relative position of the anode and cathode, as the upper cut-off voltage is defined by the cathode. Its change, without a change in the cathode capacity, is equivalent to a change in the cell balancing, which is often attributed to loss of lithium inventory (LLI) [31]. The distance P1–P2 quantifies the available active anode material. The peak height P2–P3 is a quantifier for HLD, as a more pronounced change in voltage slope correlates with a more homogeneous particle lithiation on the anode [15].

The evolution of the P1–P2 revealed that capacity lost during the phases of strong capacity loss followed by a recovery (marker 1,3,4) was linked to a loss of active anode material that was fully recovered. The explanation was that the reduction of the HLD would render some parts of the anode impossible to lithiate or delithiate. This hypothesis was confirmed by the simultaneous decrease of P2–P3 which indicates the HLD. At the same time, the value of P1 dropped as well but did not recover directly. This loss of lithium inventory was also notable in the model as increased capacity loss due to the transfer of lithium to the AOH. In the case of the deviation at marker 2, the recovery of the anode active material played a minor role, but the homogeneity indicator P2–P3 showed a strong increase, combined with an increase in the values of P1. The increase in P1 was consistent with the increase in the model, where it originated from lithium recovered from the AOH. In all four cases, the deviation between modelled and measured capacity trajectory showed an influence of HLD, missing in the model, while changes in the trajectory trends in the model were consistent with changes in the cell balancing (P1). Further reasons for deviation could be missing integration of path dependency in mixes of cyclic and calendaric ageing, which needs to be considered especially at higher C-rates [5,9].

4.6. Separation reversible and irreversible LLI

From the model equation (3) the AOH SOC can be derived by the cumulation of the transferred lithium (Fig. 8(a)). Using the values of the lithium transferred from and to the AOH returned by the model equation (3) directly (Fig. 8(b)) we were able to make a better interpretation of the changes in the value P1 linked to LLI. The most prominent LLI causes are SEI growth, irreversible plating and deactivation of lithiated active material [31,32]. Only considering these causes would explain an irreversible LLI but not the increases in the value of P1 (change of P1 > 0 in Fig. 8(b)). Hence, the reversible exchange of lithium with the AOH needed to be considered. Using the cumulated gained lithium transferred from the AOH to the active anode at each CU we calculated the irreversible LLI. The resulting values for the irreversible LLI (red dotted curve in Fig. 8(b)) were all below zero. Thus, with the help of the AOH model, we separated reversible from irreversible LLI.

5. Conclusion

In the initial investigation, we demonstrated that the OCV is influenced by the lithium transferred between the active anode and the AOH. Depending on its size, the AOH can influence the OCV on a time scale from a few days to several months. This finding was

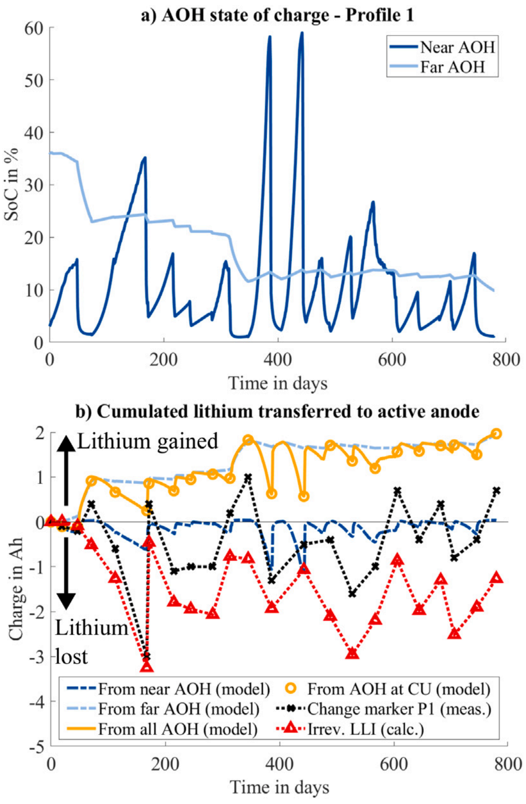

Fig. 8. Simulated evolution of the SoC of the AOH. The model provides separated values for the overhang area near and far from the active anode part. The lithium transferred from the AOH allows to calculate the LLI adjusted by the lithium stored in the AOH.

used to model the effect of the AOH on the LLI and the related cell balancing. The created model was integrated into an electrical–thermal ageing model, enabling for the first time the simulation of reversible capacity loss in a comprehensive LIB ageing model. With the sole input of a current load profile, the model allowed a long-term simulation of LIBs including electric, thermal, and ageing behaviour. The ability of the model to simulate the AOH effect on the ageing trajectory allowed us to improve the model parameters by reevaluating the initial ageing parametrisation data. We simulated the ageing tests and used the model error as input for Bayesian optimisation of the ageing model parameters. This approach led to a drastic reduction of the model error. We further improved the ageing model by adding a cyclic temperature dependency, which was also parametrised through Bayesian optimisation. The improvements in the model accuracy were confirmed by the simulation of two verification profiles including a variety of ageing conditions and phases of capacity recovery. A detailed analysis of the remaining deviation between the ageing trajectory of the verification data and of the ageing model showed the pertinence of the AOH simulation and also the model's limitations. The remaining deviation could be attributed to the effect of HLD on reversible capacity loss. Integrating the HLD as a model feature, considering the impact of temperature on the AOH model, as well as integrating the capacity rollover are potential paths for future improvements. Further, as only two cell samples were aged with verification profiles, a certain contingency could not be excluded from the small deviation between the predicted and the measured ageing trajectory. This is especially true considering the high cell-to-cell variation that was observed for cyclic ageing [33]. Hence, in future work, model verification should be done with more cell samples and growing cell-to-cell variation over ageing should be integrated into the model. Undoubtedly, the proposed model is a powerful tool for the rapid simulation of load profiles and the evaluation of their impact on the ageing of LIB. The speed, the rather simple parametrisation, and the accuracy can be leveraged in scientific as well as engineering works on LIB.

CRediT authorship contribution statement

Felix Hildenbrand: Conceptualization, Methodology, Formal analysis, Investigation, Data curation, Software, Writing – original draft, Visualization. **Dominik Ditscheid:** Data curation, Software, Methodology, Investigation, Writing – review & editing. **Elias Barbers:** Methodology, Investigation, Data curation, Software, Writing – review & editing. **Dirk Uwe Sauer:** Supervision, Funding acquisition, Writing – review & editing.

Declaration of competing interest

The authors declare the following financial interests/personal relationships which may be considered as potential competing interests: Felix Hildenbrand reports financial support was provided by Federal Ministry of Education and Research Berlin Office.

Data availability

The authors do not have permission to share data.

Acknowledgements

The authors gratefully acknowledge the financial support by ENGIE Laborelec, Belgium and by the Federal Ministry of Education and Research, Germany through the projects BALd (BMBF 03XP0320A). The authors specially thank Mark Junker and Gereon Stahl for the support with the cell disassembly and the fruitful scientific discussions.

References

[1] Ecker M, Nieto N, Käbitz S, Schmalstieg J, Blanke H, Warnecke A, et al. Calendar and cycle life study of Li(NiMnCo)O2-based 18650 lithium-ion batteries. J Power Sources 2014;248:839–51. http://dx.doi.org/10.1016/j.jpowsour.2013.09.143.

[2] Schmalstieg J, Käbitz S, Ecker M, Sauer DU. A holistic aging model for Li(NiMnCo)O2 based 18650 lithium-ion batteries. J Power Sources 2014;257:325–34. http://dx.doi.org/10.1016/j.jpowsour.2014.02.012.

[3] Schuster SF, Bach T, Fleder E, Müller J, Brand M, Sextl G, et al. Nonlinear aging characteristics of lithium-ion cells under different operational conditions. J Energy Storage 2015;1:44–53. http://dx.doi.org/10.1016/j.est.2015.05.003.

[4] Naumann M, Schimpe M, Keil P, Hesse HC, Jossen A. Analysis and modeling of calendar aging of a commercial LiFePO4/Graphite cell. J Energy Storage 2018;17:153–69. http://dx.doi.org/10.1016/j.est.2018.01.019.

[5] Epding B, Rumberg B, Jahnke H, Stradtmann I, Kwade A. Investigation of significant capacity recovery effects due to long rest periods during high current cyclic aging tests in automotive lithium ion cells and their influence on lifetime. J Energy Storage 2019;22:249–56. http://dx.doi.org/10.1016/j.est.2019.02.015.

[6] Naumann M, Spingler FB, Jossen A. Analysis and modeling of cycle aging of a commercial LiFePO4/graphite cell. J Power Sources 2020;451:227666. http://dx.doi.org/10.1016/j.jpowsour.2019.227666.

[7] Lucu M, Martinez-Laserna E, Gandiaga I, Liu K, Camblong H, Widanage W, et al. Data-driven nonparametric Li-ion battery ageing model aiming at learning from real operation data – Part A: Storage operation. J Energy Storage 2020;30:101409. http://dx.doi.org/10.1016/j.est.2020.101409.

[8] Lucu M, Martinez-Laserna E, Gandiaga I, Liu K, Camblong H, Widanage W, et al. Data-driven nonparametric Li-ion battery ageing model aiming at learning from real operation data - Part B: Cycling operation. J Energy Storage 2020;30:101410. http://dx.doi.org/10.1016/j.est.2020.101410.

[9] Raj T, Wang AA, Monroe CW, Howey DA. Investigation of path-dependent degradation in lithium-ion batteries**. Batter Supercaps 2020;3(12):1377–85. http://dx.doi.org/10.1002/batt.202000160.

[10] Lewerenz M, Fuchs G, Becker L, Sauer DU. Irreversible calendar aging and quantification of the reversible capacity loss caused by anode overhang. J Energy Storage 2018;18:149–59. http://dx.doi.org/10.1016/j.est.2018.04.029.

[11] Gyenes B, Stevens DA, Chevrier VL, Dahn JR. Understanding anomalous behavior in Coulombic efficiency measurements on Li-ion batteries. J Electrochem Soc 2015;162(3):A278–83. http://dx.doi.org/10.1149/2.0191503jes.

[12] Lewerenz M, Münnix J, Schmalstieg J, Käbitz S, Knips M, Sauer DU. Systematic aging of commercial LiFePO4|Graphite cylindrical cells including a theory explaining rise of capacity during aging. J Power Sources 2017;345:254–63. http://dx.doi.org/10.1016/j.jpowsour.2017.01.133.

[13] Wilhelm J. Cycling capacity recovery effect: A Coulombic efficiency and post-mortem study. J Power Sources 2017;12.

[14] Burrell R. Communication—Identifying and managing reversible capacity losses that falsify cycle ageing tests of lithium-ion cells. J Electrochem Soc 2020;7.

[15] Lewerenz M, Sauer DU. Evaluation of cyclic aging tests of prismatic automotive LiNiMnCoO2-Graphite cells considering influence of homogeneity and anode overhang. J Energy Storage 2018;18:421–34. http://dx.doi.org/10.1016/j.est.2018.06.003.

[16] Lewerenz M, Dechent P, Sauer DU. Investigation of capacity recovery during rest period at different states-of-charge after cycle life test for prismatic Li(Ni1/3Mn1/3Co1/3)O2-graphite cells. J Energy Storage 2019;21:680–90. http://dx.doi.org/10.1016/j.est.2019.01.004.

[17] Fath JP, Alsheimer L, Storch M, Stadler J, Bandlow J, Hahn S, et al. The influence of the anode overhang effect on the capacity of lithium-ion cells – a 0D-modeling approach. J Energy Storage 2020;29:101344. http://dx.doi.org/10.1016/j.est.2020.101344.

[18] Hüfner T, Oldenburger M, Bedürftig B, Gruhle A. Lithium flow between active area and overhang of graphite anodes as a function of temperature and overhang geometry. J Energy Storage 2019;24:100790. http://dx.doi.org/10.1016/j.est.2019.100790.

[19] Warnecke A. Degradation mechanisms in NMC-based lithium-ion batteries. vol. 105, Aachen: Aachener Beiträge des ISEA; 2017, http://dx.doi.org/10.18154/RWTH-2017-09646.

[20] Schmalstieg J. Physico-Electrochemical Simulation of Lithium-Ion Batteries : Implementation, Parametrization and Application. vol. 96, Aachen: Aachener Beiträge des ISEA; 2017, http://dx.doi.org/10.18154/RWTH-2017-04693.

[21] Rücker F, Schoeneberger I, Wilmschen T, Sperling D, Haberschusz D, Figgener Ja. Self-sufficiency and charger constraints of prosumer households with vehicle-to-home strategies. Appl Energy 2022;317:119060. http://dx.doi.org/10.1016/j.apenergy.2022.119060.

[22] Hust F, Barbers E, Hildenbrand F. ISEA framework. 2022, https://git.rwth-aachen.de/isea/framework,

[23] Hust FE. Physico-chemically motivated parameterization and modelling of real-time capable lithium-ion battery models - a case study on the Tesla model S battery. vol. 120, Aachen: Aachener Beiträge des ISEA; 2019, http://dx.doi.org/10.18154/RWTH-2019-00249.

[24] Attia PM, Bills AA, Brosa Planella F, Dechent P, dos Reis G, Dubarry M, et al. Review—“Knees” in lithium-ion battery aging trajectories. J Electrochem Soc 2022. http://dx.doi.org/10.1149/1945-7111/ac6d13.

[25] Montaru M, Fiette S, Koné J-L, Bultel Y. Calendar ageing model of Li-ion battery combining physics-based and empirical approaches. J Energy Storage 2022;51:104544. http://dx.doi.org/10.1016/j.est.2022.104544.

[26] Rasmussen CE, Williams CKI. Gaussian processes for machine learning. Adaptive Computation and Machine Learning, Cambridge, Mass: MIT Press; 2006, http://dx.doi.org/10.7551/mitpress/3206.001.0001.

[27] Zilberman I, Sturm J, Jossen A. Reversible self-discharge and calendar aging of 18650 nickel-rich, silicon-graphite lithium-ion cells. J Power Sources 2019;425:217–26. http://dx.doi.org/10.1016/j.jpowsour.2019.03.109.

[28] Zulke AA, Li Y, Keil P, Burrell R, Nagarathinam M, Mercer MP, et al. High-energy NCA cells on idle: Anode versus cathode driven side reactions. Batteries & Supercaps 2021. http://dx.doi.org/10.1002/batt.202100046, batt.202100046.

[29] Waldmann T, Wilka M, Kasper M, Fleischhammer M, Wohlfahrt-Mehrens M. Temperature dependent ageing mechanisms in lithium-ion batteries – A post-mortem study. J Power Sources 2014;262:129–35. http://dx.doi.org/10.1016/j.jpowsour.2014.03.112.

[30] Werner D, Paarmann S, Wiebelt A, Wetzel T. Inhomogeneous temperature distribution affecting the cyclic aging of Li-ion cells. Part II: Analysis and correlation. Batteries 2020;6(1):12. http://dx.doi.org/10.3390/batteries6010012.

[31] Birkl CR, Roberts MR, McTurk E, Bruce PG, Howey DA. Degradation diagnostics for lithium ion cells. J Power Sources 2017;341:373–86. http://dx.doi.org/10.1016/j.jpowsour.2016.12.011.

[32] Vetter J, Novák P, Wagner M, Veit C, Möller K-C, Besenhard J, et al. Ageing mechanisms in lithium-ion batteries. J Power Sources 2005;147(1–2):269–81. http://dx.doi.org/10.1016/j.jpowsour.2005.01.006.

[33] Baumhöfer T, Brühl M, Rothgang S, Sauer DU. Production caused variation in capacity aging trend and correlation to initial cell performance. J Power Sources 2014;247:332–8. http://dx.doi.org/10.1016/j.jpowsour.2013.08.108.